Proportional-Integral (PI) Compensator Design of Duty-Cycle-Controlled Buck LED Driver

Marn-Go Kim, *Member, IEEE*

***Abstract*—A discrete time-domain modeling and design for the duty-cycle-controlled buck light-emitting diode (LED) driver is presented in this paper. The discrete time-domain equation representing the buck LED driver is derived and linearized about the equilibrium state. Also the switching control law, the proportional-integral (PI) compensator is used here as an example of the error amplifier, is linearized about the equilibrium state. The linearized buck LED driver and the control law are then combined to arrive at a linearized duty-cycle-controlled buck LED driver. The root-locus method is employed to analyze the dynamic performance of the closed-loop system. Based on the modeling result, a practical design equation for the PI compensator is derived. Experimental results are presented to verify the validity of the proposed PI compensator design.**

***Index Terms*—Discrete time-domain modeling, duty-cycle-controlled buck light-emitting diode (LED) driver, error amplifier, proportional-integral (PI) compensator design, root-locus stability analysis.**

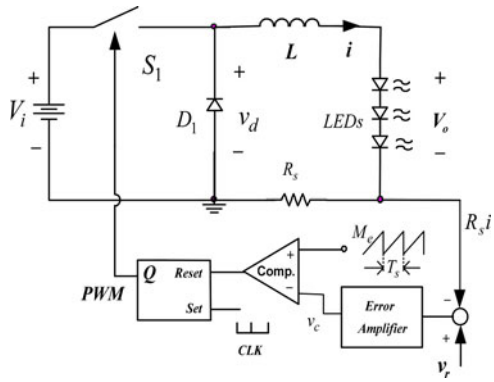

Fig. 1. Duty-cycle-controlled buck LED driver with constant-frequency controller.

I. Introduction

OVER the past few years, light-emitting diode (LED) technology has emerged as a promising technology for residential, automotive, decorative, and medical applications. This is mainly caused by the enhanced efficiency, energy savings and flexibility, and the long lifetime. Today, LEDs are available for various colors and they are suitable for white illumination [1].

The luminous flux of LEDs is mostly determined by the LED forward current. Controlling the current accurately is a challenge when each LED has a large manufacturing tolerance in its forward voltage [2]. Therefore, the regulated constant current control is needed to achieve constant brightness of LEDs [3], [4]. Recently, many works, which include power factor correction methods [5]–[9], current sharing for LED strings [10]–[14], and thermal design [15], have been done for power LED applications.

Small-signal linearized modeling for the current regulated LED driver is of crucial importance in many applications not only for assessing stability and dynamic characteristics but for designing compensators. Numerous attempts have been made to characterize the switching converter system. The average concept is successfully used in the modeling of power converters [16], [17]. The low-frequency response can be well predicted by the average models. However, one common issue of the average models is that they cannot predict subharmonic oscillations in current-mode control. Exact discrete-time model [18] can accurately predict responses. This numerical technique is not useful to be used in practical design. In order to extend the validation of the average models to the high-frequency range, modified average models are proposed based on the results of discrete-time analysis and sampled-data analysis [19], [20]. All mentioned modeling approaches are related to voltage regulated converters. Very little work has been done in the area of modeling and control to improve dynamic performance of the current regulated LED driver [21]–[23].

In this paper, the systematic discrete time-domain approach [24]–[27] is adapted to modeling and designing feedback compensator for the duty-cycle-controlled buck LED driver shown in Fig. 1. Root-locus analysis is used to derive the stability boundaries and the practical design equation for selecting the optimum proportional-integral (PI) gains of the error amplifier. Experimental results are presented to confirm the validity of the proposed design method.

II. Discrete Time-Domain Modeling of the Duty-Cycle-Controlled Buck LED Driver

The discrete time-domain model is carried out under the following assumptions.

1) all components are ideal;
2) the output voltage V_o and the input voltage V_i are constant;
3) the loading effect of the feedback loop on the power stage can be neglected.

Manuscript received April 14, 2014; revised June 5, 2014; accepted July 7, 2014. Date of publication July 21, 2014; date of current version February 13, 2015. This work was supported by a Research Grant of Pukyong National University under Project CD2014-0293. Recommended for publication by Associate Editor K.-H. Chen.

The author is with the Department of Control and Instrumentation Engineering, Pukyong National University, Busan 608-737, Korea (e-mail: mgkim@pknu.ac.kr).

Color versions of one or more of the figures in this paper are available online at http://ieeexplore.ieee.org.

Digital Object Identifier 10.1109/TPEL.2014.2341253

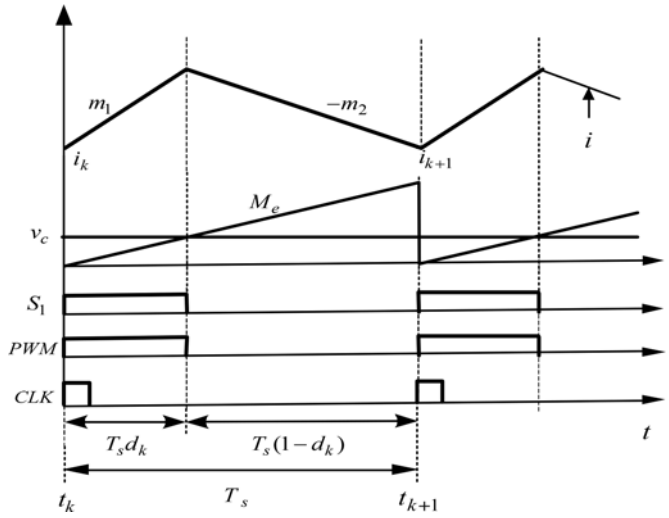

Fig. 2. Key theoretical waveforms of Fig. 1.

A. Discrete Time-Domain Representation

In Fig. 1, the clock signal is applied to the Set input, and initiates the switch ON-time uniformly at the switching frequency $f_s = 1/T_s$. The switch ON-time is terminated when the ramp signal with slope M_e reaches the control signal v_c.

The relationship is determined at the comparator input, whose detailed waveforms are shown in Fig. 2. One comparator input carries the control voltage v_c and the other input carries the ramp voltage signal. The instantaneous inductor current has a positive ramp of slope $+m_1$ when the power switch is ON and a negative ramp of slope $-m_2$ when the switch is OFF, and the duty ratio d_k is determined by intersection of the two comparator inputs, which is given by

$$M_e T_s d_k = v_c|_{t=t_k+T_s d_k} \tag{1}$$

where M_e is the slope of the sawtooth ramp signal.

This switching control law [25] is termed as the threshold condition in [24] or the constraint condition in [18].

At the switching instant, the control signal v_c for the PI compensator can be represented as [22]

$$\begin{aligned} v_c|_{t=t_k+T_s d_k} = \; & v_r + k_p\{v_r - R_s(i_k + m_1 T_s d_k)\} + v_k \\ & + k_i R_s T_s d_k \left\{ \frac{v_r}{R_s} - \left(i_k + m_1 \frac{T_s d_k}{2} \right) \right\} \end{aligned} \tag{2}$$

where the proportional gain k_p is $\frac{R_1}{R_2}$ and the integral gain k_i is $\frac{1}{R_2 C_1}$.

Using (1) and (2), the switching control law can be described as

$$\begin{aligned} & (k_p + k_i T_s d_k) i_k - \frac{1}{R_s} v_k \\ & + \left(k_p m_1 T_s + k_i T_s \frac{m_1 T_s d_k}{2} + \frac{M_e T_s}{R_s} \right) d_k \\ & - \frac{(1 + k_p + k_i T_s d_k)}{R_s} v_r = 0. \end{aligned} \tag{3}$$

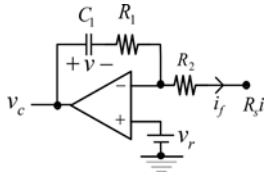

Fig. 3. PI error amplifier circuit.

The discrete time-domain equation for the inductor current can be represented as

$$i_{k+1} = i_k + m_1 T_s d_k - m_2 T_s (1 - d_k) \tag{4}$$

where i_k is the inductor current at $t = t_k$ and i_{k+1} is the inductor current at $t = t_{k+1}$.

As an example of the error amplifier circuit, the PI compensator is used here as shown in Fig. 3. A discrete time-domain equation for the capacitor voltage v can be written as

$$\begin{aligned} v_{k+1} &= v_k + \frac{1}{C_1} \int_{t_k}^{t_{k+1}} \frac{(v_r - R_s i)}{R_2} dt \\ &= v_k + k_i R_s T_s \left(\frac{v_r}{R_s} - i_{\mathrm{avg},k} \right) \end{aligned} \tag{5}$$

where

$$\begin{aligned} i_{\mathrm{avg},k} = \; & \frac{1}{T_s} \int_{t_k}^{t_{k+1}} i dt = \left(i_k + m_1 \frac{T_s d_k}{2} \right) \cdot d_k \\ & + \left\{ i_k + m_1 T_s d_k - m_2 \frac{T_s (1 - d_k)}{2} \right\} \cdot (1 - d_k). \end{aligned}$$

B. Equilibrium State

In the steady-state, setting $i_{k+1} = i_k = I$, $v_{k+1} = v_k = V$, $m_1 = M_1$, $m_2 = M_2$, $i_{\mathrm{avg},k} = I_{\mathrm{avg}}$, $v_r = V_r$, and $d_k = D$, (4) and (5) can be written as

$$M_1 T_s D = M_2 T_s (1 - D) \tag{6a}$$

$$I_{\mathrm{avg}} = V_r / R_s = I + M_1 T_s D / 2 \tag{6b}$$

where $D = V_o/V_i$, $M_1 = (V_i - V_o)/L$ and $M_2 = V_o/L$.

C. Linearization About the Equilibrium State

Equation (4) can be linearized about the equilibrium state as

$$\delta i_{k+1} = \delta i_k + (M_1 + M_2) T_s \cdot \delta d_k. \tag{7}$$

Similarly, (5) can also be linearized about the equilibrium state using the steady-state conditions (6a) and (6b)

$$\begin{aligned} \delta v_{k+1} = \; & -k_i R_s T_s \cdot \delta i_k + \delta v_k - k_i R_s T_s M_1 T_s \cdot \delta d_k \\ & + k_i T_s \cdot \delta v_r. \end{aligned} \tag{8}$$

The switching condition (3) can be rewritten compactly as

$$f[i_k, v_k, d_k, v_r] = 0. \tag{9}$$

Using (9), the linearized switching control law about the equilibrium state can be described as

$$\frac{\partial f}{\partial i_k}|_* \cdot \delta i_k + \frac{\partial f}{\partial v_k}|_* \cdot \delta v_k + \frac{\partial f}{\partial d_k}|_* \cdot \delta d_k + \frac{\partial f}{\partial v_r}|_* \cdot \delta v_r = 0 \tag{10}$$

where

$$\frac{\partial f}{\partial i_k}|_* = k_p + k_i T_s D, \frac{\partial f}{\partial v_k}|_* = -\frac{1}{R_s}$$
$$\frac{\partial f}{\partial d_k}|_* = k_p M_1 T_s + k_i T_s (I + M_1 T_s D - \frac{V_r}{R_s}) + \frac{M_e T_s}{R_s}$$
$$\frac{\partial f}{\partial v_r}|_* = -(1 + k_p + k_i T_s D)/R_s.$$

Substituting (6b) into the partial derivative of f with respect to d_k, $\frac{\partial f}{\partial d_k}|_*$ gives

$$\frac{\partial f}{\partial d_k}|_* = M_1 T_s (S_r + k_p + k_i T_s D/2) \tag{11}$$

where $S_r = M_e/(M_1 R_s) = \dfrac{M_e}{(V_o R_s/L)} \dfrac{D}{(1-D)}$.

S_r is the ratio of the external ramp slope to the ON-time slope of the current-sense waveform.

D. Combination of the Linearized System and Linearized Control Law

From (10) and (11), the following form can be derived for the linearized control law:

$$\delta d_k = -K_1 \cdot \delta i_k - K_2 \cdot \delta v_k - K_3 \cdot \delta v_r \tag{12}$$

where

$$K_1 = \frac{k_p + k_i T_s D}{M_1 T_s (S_r + k_p + k_i T_s D/2)}$$
$$K_2 = -\frac{1}{R_s M_1 T_s (S_r + k_p + k_i T_s D/2)}$$
$$K_3 = -\frac{1 + k_p + k_i T_s D}{R_s M_1 T_s (S_r + k_p + k_i T_s D/2)}.$$

Combining (7), (8), and (12) gives the following closed-loop system :

$$\delta X_{k+1} = A \cdot \delta X_k + B \cdot \delta v_r \tag{13}$$

where

$$\delta X_{k+1} = [\delta i_{k+1} \delta v_{k+1}]^T, \delta X_k = [\delta i_k \delta v_k]^T$$
$$A = \begin{bmatrix} a_{11} & a_{12} \\ a_{21} & a_{22} \end{bmatrix}, B = \begin{bmatrix} b_1 \\ b_2 \end{bmatrix}$$
$$a_{11} = 1 - (M_1 + M_2) T_s \cdot K_1 = 1 - \frac{1}{(1-D)} \frac{k_p + k_{ni} D}{(S_r + k_p + k_{ni} D/2)}$$
$$a_{12} = -(M_1 + M_2) T_s \cdot K_2 = \frac{1}{R_s} \frac{1}{(1-D)} \frac{1}{(S_r + k_p + k_{ni} D/2)}$$
$$a_{21} = -k_i R_s T_s + k_i R_s T_s M_1 T_s \cdot K_1 = R_s \frac{k_{ni}(k_{ni} D/2 - S_r)}{S_r + k_p + k_{ni} D/2}$$
$$a_{22} = 1 + k_i R_s T_s M_1 T_s \cdot K_2 = 1 - \frac{k_{ni}}{S_r + k_p + k_{ni} D/2}$$
$$b_1 = -(M_1 + M_2) T_s \cdot K_3 = \frac{1}{R_s} \frac{1}{(1-D)} \frac{1 + k_p + k_{ni} D}{(S_r + k_p + k_{ni} D/2)}$$
$$b_2 = k_i T_s + k_i R_s T_s M_1 T_s \cdot K_3 = -\frac{k_{ni}(1 + k_{ni} D/2 - S_r)}{S_r + k_p + k_{ni} D/2}$$
$$D = V_o/V_i, k_p = \frac{R_1}{R_2},\ k_{ni} = k_i T_s = \frac{T_s}{R_2 C_1},$$
$$S_r = \frac{M_e}{(V_o R_s/L)} \frac{D}{(1-D)}.$$

III. Design Guidelines

Bode plots have been commonly used to assess the stability of the closed-loop system by finding the phase margin, but these plots cannot give information on the dynamic behavior of the individual state variables. On the other hand, root-locus analysis can provide the engineer with the stability and the transient performance of the individual state variables related to the location of the roots of the characteristic equation.

To analyze the stability and dynamic characteristics of the closed-loop system, the eigenvalues of the system matrix is evaluated. The eigenvalues of A is the solutions of

$$|A - zI| = 0 \tag{14}$$

where *I* is the identity matrix. The following root-locus analysis is performed for $R_s = 1$.

The root locus as a function of the P gain k_p for $k_{ni} = 0.2$, $D = 0.45$, and $S_r = 0.82$ is shown in Fig. 4. Corresponding pole locations between the *s*-plane and the *z*-plane are shown. The eigenvalues λ_1 and λ_2 in the *z*-plane are mapped to s_1 and $\overline{s_1}$, and s_2 in the *s*-plane, respectively. Unlike the peak-current-controlled buck LED driver reported in [22], this duty-cycle-controlled buck LED driver is unstable for $k_p = 0$. The

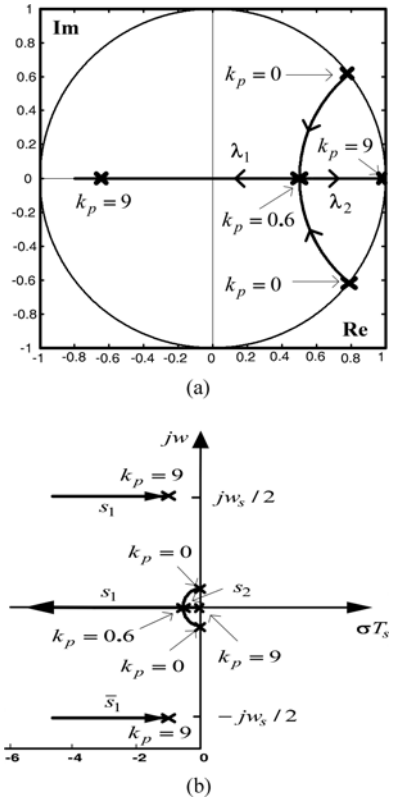

Fig. 4. Root locus as a function of the *P* gain k_p: (a) in the z-plane and (b) in the s-plane ($k_{ni} = 0.2$, $D = 0.45$, $S_r = \frac{1.0D}{1-D} = 0.82$).

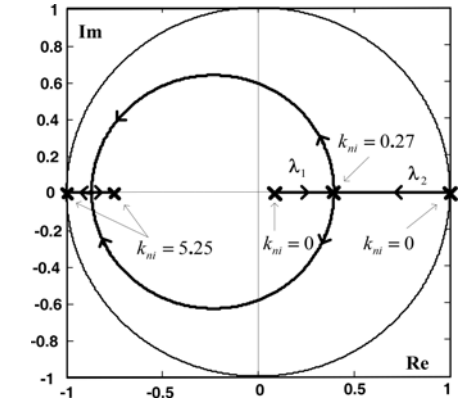

Fig. 5. Root locus as a function of the *I* gain k_{ni} ($k_p = 0.84$, $D = 0.4$, $S_r = \frac{1.5D}{1-D} = 1.0$).

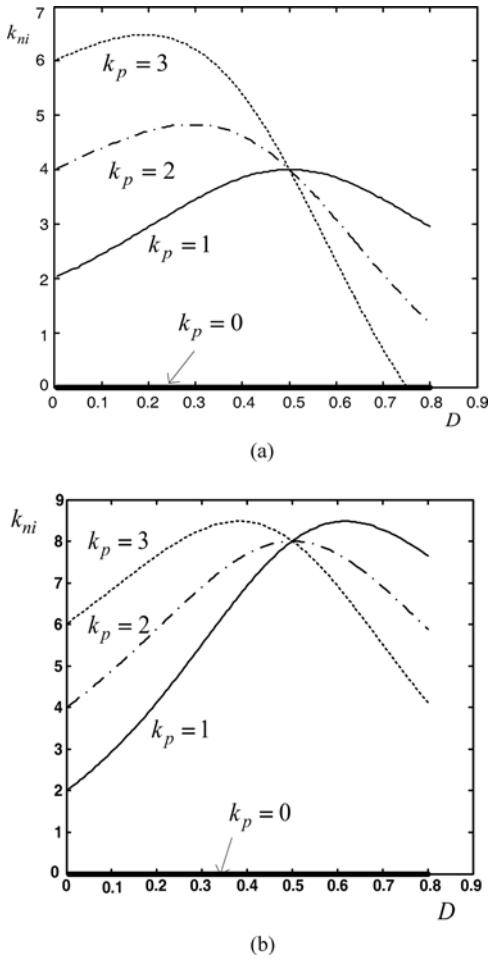

Fig. 6. Theoretical stability boundaries of k_{ni} as a function of *D*. (a) $S_r = \frac{1.0D}{1-D}$. (b) $S_r = \frac{2D}{1-D}$.

eigenvalue λ_1 is dominated by the inductor current state. The transient response of λ_1 after a disturbance is underdamped when k_p is between 0 and 0.6. At $k_p = 0.6$, the system response is critically damped. And then, λ_1 moves toward the origin of the unit circle with increasing k_p, which means the inductor current becomes faster. When k_p is greater than 0.6, the transient response of the inductor current is overdamped. Increasing k_p much further, the current response is underdamped with a natural resonant frequency equal to $f_s/2$ due to the negative real value of λ_1. On the other hand, the eigenvalue λ_2 is dominated by the capacitor voltage state of the error amplifier. The transient response of λ_2 is underdamped when k_p is between 0 and 0.6 due to the two complex roots. Then, λ_2 moves toward the unit circle with increasing k_p, which means the capacitor voltage becomes slower. The capacitor voltage is overdamped when k_p is greater than 0.6. The relationship between the s-plane poles and the z-plane poles is

$$z = e^{sT_s}|_{s=\sigma \pm jw} = e^{\sigma T_s} \underline{/ \pm wT_s}. \tag{15}$$

The detailed information about the time response of the discrete system can be found in [28].

The root locus as a function of the *I* gain k_{ni} for $k_p = 0.84$, $D = 0.4$, and $S_r = 1.0$ is shown in Fig. 5. When the *I* gain k_{ni} is increased from 0 to 0.27, the transient response is changed from overdamped to critically damped, and the overall system response becomes faster due to the slower eigenvalue λ_2 moving toward the origin of the unit circle. The transient response is underdamped when the *I* gain k_{ni} is greater than 0.27. Selecting k_{ni} greater than 5.25, the closed-loop system is unstable.

Fig. 6 shows stability boundaries of k_{ni} as a function of *D*. When k_{ni} is between zero and the stability boundary, the system

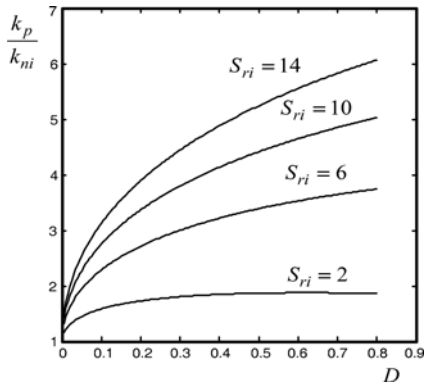

Fig. 7. PI gain curve for the critically damped response.

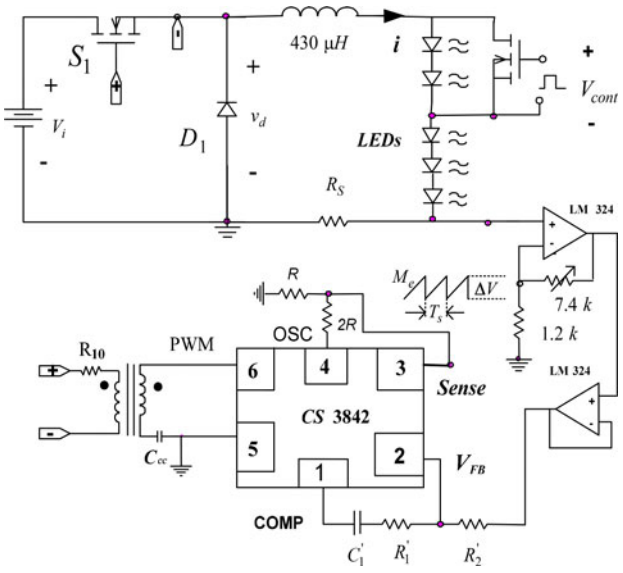

Fig. 8. Experimental circuit.

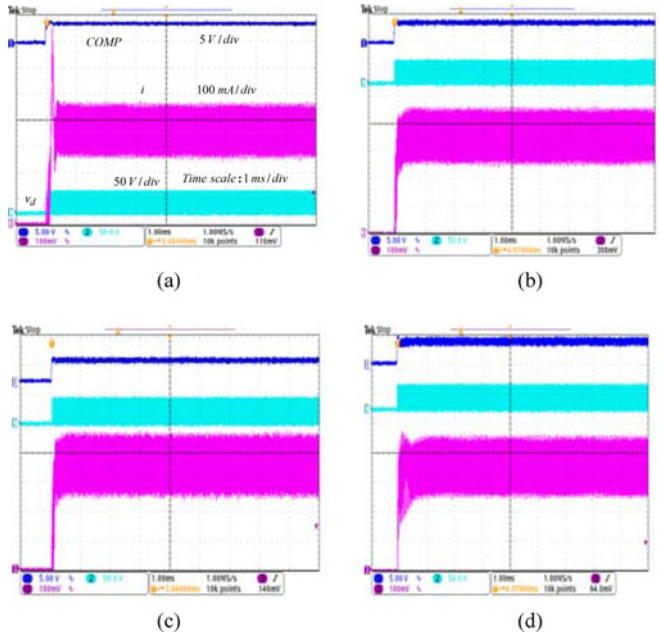

Fig. 9. Start-up transient responses with increasing proportional gain k_p ($V_i = 40\,\mathrm{V}$, $V_o \approx 16.25\,\mathrm{V}$, $k_{ni} = 0.2$, $R_2' = 12\ k$, $C_1' = 10\,\mathrm{nF}$). (a) $k_p = 0.1$ ($R_1' = 0.5\ k$). (b) $k_p = 0.84$ ($R_1' = 4.2\ k$). (c) $k_p = 1.3$ ($R_1' = 6.5\ k$). (d) $k_p = 2.0$ ($R_1' = 10\ k$).

is stable. While the peak-current-controlled buck LED driver can be stable by selecting a proper *I* gain for $k_p = 0$ [22], this duty-cycle-controlled buck LED driver is always unstable for $k_p = 0$. The stability boundary of k_{ni} is increasing with increasing k_p for $D < 0.5$. But, this stability boundary of k_{ni} is decreasing with increasing k_p for $D > 0.5$. The stable range of k_{ni} is very wide for a fixed k_p and *D*. However, the design engineer need to select the optimum k_p and k_{ni} for a good transient response instead of the simple stable gains.

In practical design, it is desirable that the transient response of the system should be critically damped or slightly overdamped to avoid an oscillatory LED current for the start-up and step load change. The system response is critically damped when λ_1 is equal to λ_2. Using the condition of $(a_{11} + a_{22})^2 - 4(a_{11}a_{22} - a_{12}a_{21}) = 0$, and considering $k_p > 0$, the border equation between the underdamped and overdamped cases can be derived as

$$\frac{k_p}{k_{ni}} = (1-2D) + \sqrt{2(1-D)(2S_r/k_{ni} - D)} = (1-2D) + \sqrt{2(1-D)(S_{ri}\frac{2D}{1-D} - D)} \tag{16}$$

where $S_{ri} = \dfrac{M_e}{(V_o R_s/L)}\dfrac{1}{k_{ni}}$.

Using (16), PI gain curve for the critically damped response is shown in Fig. 7. The system response is underdamped when k_p is less than the value on the curve, and overdamped when k_p is greater than the value on the curve. Generally, the boundary value of k_p between underdamped and overdamped responses is increasing with increasing k_{ni} for the same *D* and S_r. The *P* gain for nonoscillatory response is determined at the maximum *D* for a range of operation. Selecting k_p slightly greater than or equal to the value on the curve at the maximum *D* of an operating range, a satisfactory transient response can be achieved. In other words, when *D* varies between 0.2 and 0.6, the *P* gain k_p slightly greater than or equal to 0.8 at $D_{\max} = 0.6$ can be chosen for $k_{ni} = 0.2$ and $S_{ri} = 7.5$. Because designing k_p according to the border equation of a lower *D* results in an oscillatory transient response at $D_{\max}$.

IV. Experimental Evaluation

For performance evaluations, a prototype converter has been constructed as shown in Fig. 8. The constant switching frequency is 100 kHz. The normal operating range of *D* in the

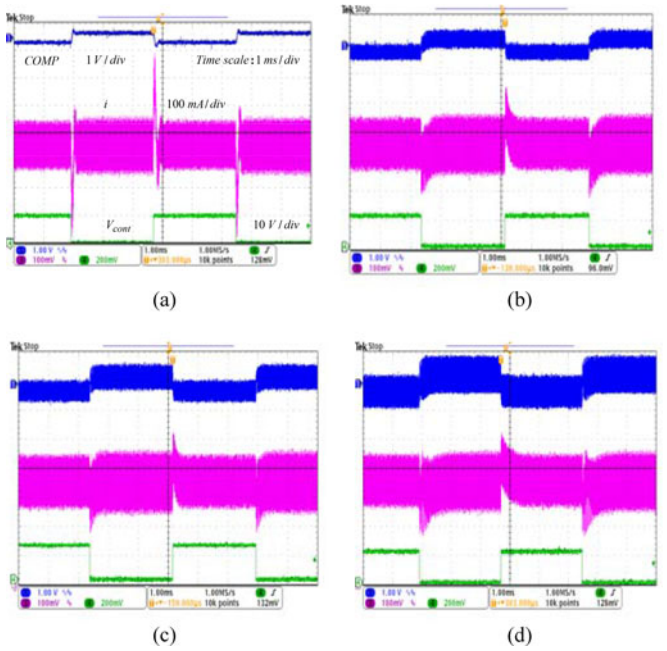

Fig. 10. Transient responses for step load change between 3 and 5 LEDs ($V_i = 40$ V, $k_{ni} = 0.2$, $R_2' = 12\ k$, $C_1' = 10$ nF). (a) $k_p = 0.1$ ($R_1' = 0.5\ k$). (b) $k_p = 0.84$ ($R_1' = 4.2\ k$). (c) $k_p = 1.3$ ($R_1' = 6.5\ k$). (d) $k_p = 2.0$ ($R_1' = 10\ k$).

converter is between 0.2 and 0.6. In the experiment, the ramp peak-to-peak amplitude ΔV is $1.7/3 \approx 0.567$ V, which is generated with $\frac{1}{3}$ of the oscillator peak-to-peak amplitude 1.7 V [29]. The ramp slope M_e is $\Delta V/T_s = 0.567 \times 100 \times 10^3$. The control IC is CS3842. S is IRF 840 and D_1 is DSEI12-06A. Here, we use pure-white LEDs, Z-POWER w42182, which has a typical current of 350 mA. This LED forward voltage varies from 3.0 to 4.0 V, for a nominal of 3.25 V [2]. The output voltage is approximately (3.25 V $\times$ 5 LEDs in series) 16.25 V. S_{ri} is $\frac{M_e}{(V_o R_s/L)} \frac{1}{k_{ni}} = \frac{0.567 \times 100 \times 10^3}{\{16.25 \times 1/(430 \times 10^{-6})\}} \frac{1}{k_{ni}} = \frac{1.5}{k_{ni}}$ for $R_s = 1\Omega$, and S_r is $\frac{1.5D}{1-D}$. Setting $k_{ni} = 0.2$, S_{ri} is 7.5. From (16), $\frac{k_p}{k_{ni}}$ is $(1-2D) + \sqrt{2(1-D)(S_{ri}\frac{2D}{1-D} - D)} = 4.0$ for the maximum $D = 0.6$. The designed k_p is selected to be 0.84, which is slightly greater than 0.8 for $k_{ni} = 0.2$. The integral gain is $k_i = k_{ni}/T_s = 0.2 \times 100 \times 10^3 = 20\,000$. The PI gains are distributed throughout the feedback path between the current sense and the comparator input. The gain of LM324 is $\frac{1.2k+7.4k}{1.2k} = 7.16$. The function of LM 324 is converting the sensed $R_s i$ to the internal reference voltage of the error amplifier. The average value of the output voltage of LM 324 is equal to the reference voltage of the error amplifier input, which is 2.5 V in the datasheet [29]. From the datasheet, the internal gain between COMP and the comparator input is $\frac{1}{3}$. The overall proportional gain k_p and integral gain k_i are $\frac{7.16}{3} \times \frac{R_1'}{R_2'}$ and $\frac{7.16}{3} \times \frac{1}{R_2' C_1'}$, respectively. For the designed integral gain $k_i = 20\,000$, the values of R_2' and C_1' are chosen to be 12 k and 0.01 μF. For the designed proportional gain $k_p = 0.84$, the value of R_1' is chosen to be 4.2 k.

With five LEDs connected in series, which provides a typical loading voltage of approximately (3.25 V $\times$ 5 LEDs in series) 16.25 V, the LED currents are measured for start-up transience with increasing P gain as shown in Fig. 9. As the P gain increases from $k_p = 0.1$ to $k_p = 1.3$, the transient response of the LED current changes from underdamped to overdamped response, and then, to a slower and poor transient response due to

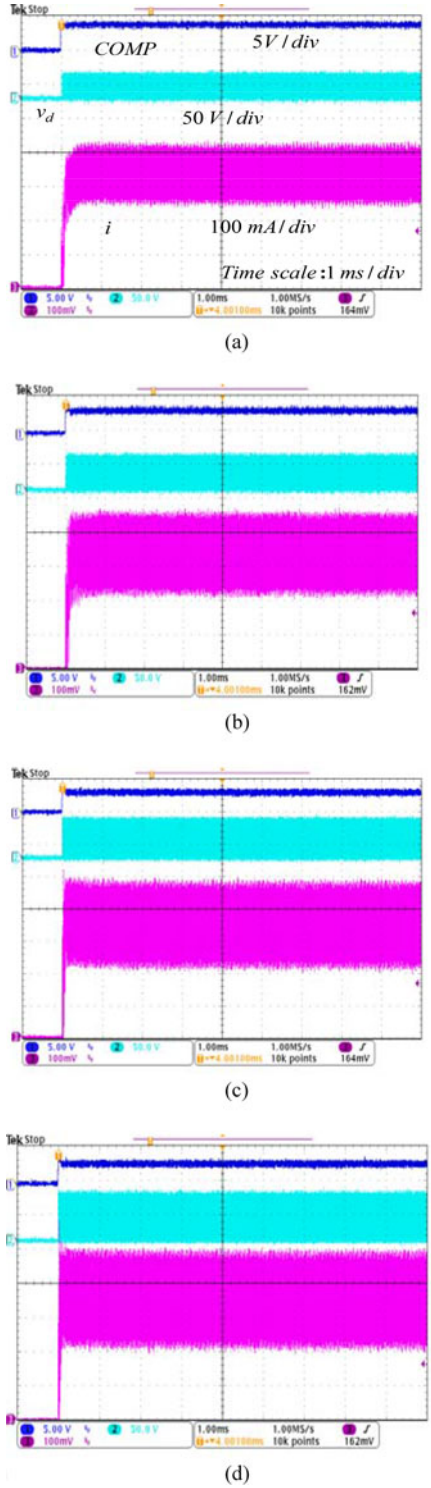

Fig. 11. Start-up transient responses with increasing the input voltage ($V_o \approx 16.25$ V, $k_p = 0.84$, $k_{ni} = 0.2$). (a) $V_i = 30\,V$ ($S_r \approx 1.77$). (b) $V_i = 50\,V$ ($S_r \approx 0.72$) (c) $V_i = 60\,V$ ($S_r \approx 0.56$) (d) $V_i = 70\,V$ ($S_r \approx 0.45$).

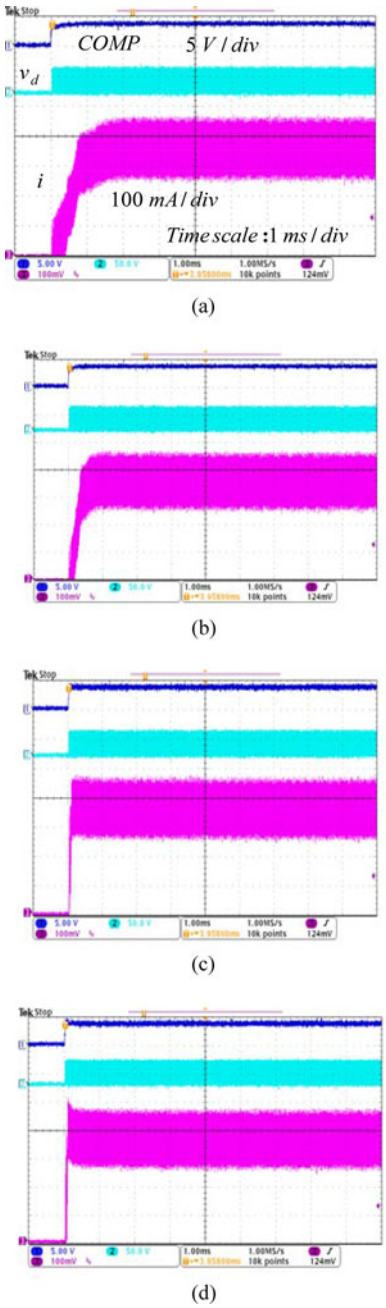

Fig. 12. Start-up transient responses with increasing integral gain k_{ni}(V_i = 40 V, $V_o \approx 16.25$ V, $k_p = 0.84$, $R_1' = 4.2\ k$, $R_2' = 12\ k$). (a) $k_{ni} = 0.02$ ($C_1' = 0.1\ uf$). (b) $k_{ni} = 0.1$ ($C_1' = 20\ nf$). (c) $k_{ni} = 0.29$ ($C_1' = 6.8\ nf$). (d) $k_{ni} = 0.38$ ($C_1' = 5.3\ nf$).

the slower error amplifier state for $k_p = 2.0$. This experimental response shows a good agreement with the prediction of the root-locus analysis.

Fig. 10 shows the measured COMP, which is the PI error amplifier output, and i. The output load is changed between three and five LEDs in series by the control input $V_{\rm cont}$, which results in the step change of the output voltage, approximately between 9.75 and 16.25 V. From this figure, it can be said that the system response is good for a value of k_p between 0.84 and 1.3, which is slightly greater than 0.8 for the critically

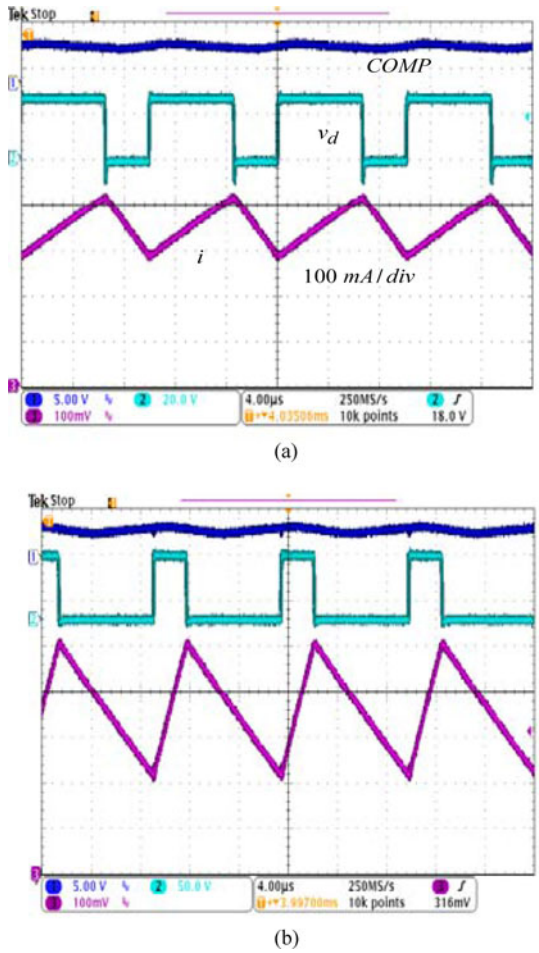

Fig. 13. Steady-state waveforms with increasing the input voltage ($V_o \approx 16.25$ V, $k_p = 0.84$, $k_{ni} = 0.2$). (a) $V_i = 27\,V$. (b) $V_i = 70\,V$.

damped response at the maximum $D = 0.6$. When the input voltage varies from 30 to 70 V, the start-up transient responses for $k_p = 0.84$ and $k_{ni} = 0.2$ are shown in Fig. 11. The ON-time current-sense slope changes according to the input voltage variation, which results in the variation of S_r. In this experiment, S_r is $\frac{1.5D}{1-D} \approx \frac{1.5}{V_i/16.25-1}$. The designed PI gains can provide the system with good start-up responses for the wide range of input voltage.

Start-up transient responses for the increase of integral gain k_{ni} are shown in Fig. 12. Increasing k_{ni} from 0.02 to 0.38, the system changes from overdamped to critically damped, and then, to underdamped. These results show a good agreement with the prediction of the root-locus analysis in Fig. 5.

Fig. 13 shows steady-state waveforms with increasing the input voltage. This experimental result shows that the average LED current of the duty-cycle-controlled buck converter does not vary for a wide range of input voltage.

V. Conclusion

A discrete time-domain modeling and analysis for the duty-cycle-controlled buck LED driver has been presented. The discrete time-domain equation that represents the static and

dynamic behavior of the buck converter is derived and linearized about the equilibrium state of the buck converter. Also the duty cycle control law is linearized about the equilibrium state. The linearized buck converter and the linearized duty cycle control law are then combined to arrive at a linearized duty-cycle-controlled LED driver.

The PI compensator is used as an example of the error amplifier. Increasing P gain from zero, the transient response of the inductor current state changes from underdamped to overdamped, and then, to underdamped with natural resonant frequency equal to half of the switching frequency. The duty-cycle-controlled buck LED driver is always unstable for $k_p = 0$. The stable integral gain range is very wide for a given P gain. In practical design, it is desirable that the transient response of the inductor current should be critically damped or slightly overdamped to avoid an oscillatory LED current. Based on this concept, the PI gains can be determined at the maximum D in the range of operating region. Therefore, for a good transient response, the P gain k_p slightly greater than or equal to $k_{ni}\{(1-2D_{\max}) + \sqrt{2(1-D_{\max})(S_{ri}\frac{2D_{\max}}{1-D_{\max}} - D_{\max})}\}$ can be selected. Selecting the PI gains of the error amplifier according to this practical design equation is very easy and useful for the design engineer. Experimental results are presented to confirm the validity of the proposed PI compensator design.

REFERENCES

[1] D. G. Lamar, M. Arias, A. Rodriguez, A. Fernandez, M. M. Hernando, and J. Sebastian, "Design-oriented analysis and performance evaluation of a low-cost high-brightness LED driver based on flyback power factor corrector," *IEEE Trans. Ind. Electron.*, vol. 60, no. 7, pp. 2614–2626, Jul. 2013.

[2] Seoul Semiconductor Co., LTD. (2009). Z-power LED series–technical datasheet for X4218X. [Online]. Available : http://www.seoulsemicon.com/kr/html/main/

[3] C. B. Park, B. H. Choi, J. P. Cheon, and C. T. Rim, "Robust active LED driver with high power factor and low total harmonic distortion compatible with a rapid-start ballast," *J. Power Electron.*, vol. 14, no. 2, pp. 226–236, Mar. 2014.

[4] H. H. Chou, Y. S. Hwang, and J. J. Chen, "An adaptive output current estimation circuit for a primary-side controlled LED driver," *IEEE Trans. Power Electron.*, vol. 28, no. 10, pp. 4811–4819, Oct. 2013.

[5] Q. Hu and R. Zane, "Minimizing required energy storage in off-line LED drivers based on series-input converter modules," *IEEE Trans. Power Electron.*, vol. 26, no. 10, pp. 2887–2895, Oct. 2011.

[6] W. Chen and S. Y. R. Hui, "Elimination of an electrolytic capacitor in AC/DC light-emitting diode(LED) driver with high input power factor and constant output current," *IEEE Trans. Power Electron.*, vol. 27, no. 27, pp. 1598–1607, Mar. 2012.

[7] Y. X. Qin, H. S. H. Chung, D. Y. Lin, and S. Y. R. Hui, "Current source ballast for high power lighting emitting diodes without electrolytic capacitor," in *Proc. IEEE Ind. Electron. Conf.*, 2008, pp. 1968–1973.

[8] J. M. Alonso, J. Vina, D. G. Vaquero, G. Martinez, and R. Osorio, "Analysis and design of the integrated double buck-boost converter as a high-power-factor driver for power-LED lamps," *IEEE Trans. Ind. Electron.*, vol. 59, no. 4, pp. 1689–1697, Apr. 2012.

[9] F. Zhang, J. Ni, and Y. Yu, "High power factor AC-DC LED driver with film capacitors," *IEEE Trans. Power Electron.*," vol. 28, no. 10, pp. 4831–4840, Oct. 2013.

[10] Q. Luo, S. Zhi, C. Zou, W. Lu, and L. Zhou, "An LED driver with dynamic high-frequency sinusoidal bus voltage regulation for multistring applications," *IEEE Trans. Power Electron.*, vol. 29, no. 1, pp. 491–500, Jan. 2014.

[11] X. Wu, C. Hu, J. Zhang, and C. Zhao, "Series-parallel autoregulated charge-balancing rectifier for multioutput light-emitting diode driver," *IEEE Trans. Ind. Electron.*, vol. 61, no. 3, pp. 1262–1268, Mar. 2014.

[12] X. Wu, Z. Wang, and J. Zhang, "Design considerations for dual-output quasi-resonant flyback LED driver with current-sharing transformer," *IEEE Trans. Power Electron.*, vol. 28, no. 10, pp. 4820–4830, Oct. 2013.

[13] K. H. Loo, Y. M. Lai, and C. K. Tse, "Design and analysis of LCC resonant network for quasi-lossless current balancing in multistring AC-LED array," *IEEE Trans. Power Electron.*, vol. 28, no. 2, pp. 1047–1059, Feb. 2013.

[14] J. Patterson and R. Jane, "Series input modular architecture for driving multiple LEDs," in *Proc. IEEE Power Electron. Spec. Conf.*, Athens, Greece, Jun. 2008, pp. 2650–2656.

[15] S. Y. R. Hui and Y. X. Qin, "A general photo-electro-thermal theory for light emitting diode (LED) systems," *IEEE Trans. Power Electron.*, vol. 24, no. 8, pp. 1967–1976, Aug. 2009.

[16] R. D. Middlebrook, "Modeling current-programmed buck and boost regulators," *IEEE Trans. Power Electron.*, vol. 4, no. 1, pp. 36–52, Jan. 1989.

[17] G. K. Schoneman and D. M. Mitchell, "Output impedance considerations for switching regulators with current-injected control," *IEEE Trans. Power Electron.*, vol. 4, no. 1, pp. 25–35, Jan. 1989.

[18] F. C. Lee, R. P. Iwens, Y. Yu, and J. E. Triner, "Generalized computer-aided discrete-time modeling and analysis of dc-dc converters," *IEEE Trans. Ind. Electron. Contr. Instrum.*, vol. IECI-26, no. 2, pp. 58–69, May 1979.

[19] R. B. Ridley, "A new, continuous-time model for current-mode control," *IEEE Trans. Power Electron.*, vol. 6, no. 2, pp. 271–280, Apr. 1991.

[20] F. D. Tan and R. D. Middlebrook, "A unified model for current-programmed converters," *IEEE Trans. Power Electron.*, vol. 10, no. 4, pp. 397–408, Jul. 1995.

[21] Y. S. Jung and M. G. Kim, "Time-delay effects on DC characteristics of peak current controlled power LED driver," *J. Power Electron.*, vol. 12, no. 5, pp. 715–722, Sep. 2012.

[22] M. G. Kim, "Error amplifier design of peak current controlled (PCC) buck LED driver," *IEEE Trans. Power Electron.*, vol. 29, no. 12, pp. 6789–6795, Dec. 2014.

[23] W. Feng, F. C. Lee, and P. Mattavelli, "Optimal trajectory control of LLC resonant converter for LED PWM dimming," *IEEE Trans. Power Electron.*, vol. 29, no. 2, pp. 979–987, Jan. 2014.

[24] G. C. Verghese, M. E. Elbuluk, and J. G. Kassakian, "A general approach to sampled-data modeling for power electronic circuit," *IEEE Trans. Power Electron.*, vol. PE-1, no. 2, pp. 76–89, Apr. 1986.

[25] M. G. Kim and M. J. Youn, "A discrete time domain modeling and analysis of controlled series resonant converter," *IEEE Trans. Ind. Electron.*, vol. 38, no. 1, pp. 32–40, Feb. 1991.

[26] M. G. Kim and M. J. Youn, "An energy feedback control of series resonant converter," *IEEE Trans. Power Electron.*, vol. 6, no. 3, pp. 338–345, Jul. 1991.

[27] M. G. Kim, D. S. Lee, and M. J. Youn, "A new state feedback Control of resonant converters," *IEEE Trans. Ind. Electron.*, vol. 38, no. 3, pp. 173–179, Jun. 1991.

[28] C. L. Phillips and H. T. Nagle, Jr., *Digital Control System Analysis and Design*. Englewood Cliffs, NJ, USA: Prentics-Hall, 1987, ch. 6.

[29] Cherry Semiconductor Corp. CS3842B datasheet. (2001). [Online]. Available: http://www.onsemi.com/pub/Collateral/CS3842B-D.PDF

Marn-Go Kim (S'90–M'93) received the B.S. degree in electrical engineering from Kyungpook National University, Daegu, South Korea, in 1986, and the M.S. and Ph.D. degrees in electrical engineering from the Korea Advanced Institute of Science and Technology, Daejeon, South Korea, in 1988 and 1991, respectively.

From 1991 to 1995, he was with Korea Telecom Research Center, Seoul, South Korea, where he served as the Leader of a project team for telecom power systems. From 2003 to 2004, he was a Visiting Scholar at Virginia Polytechnic Institute and State University, Blacksburg, VA, USA. Since 1995, he has been with the Department of Control & Instrumentation Engineering, Pukyong National University, Busan, Korea, where he is currently a Professor. His research interests include modeling, analysis, and control of dc/dc converters, power electronics applications, and soft switching converters.

Dr. Kim is a Member of the Korean Institute of Power Electronics and the Korean Institute of Electrical Engineers.